Int J CARS (2009) 4:53–63
DOI 10.1007/s11548-008-0259-9

ORIGINAL ARTICLE

Development and validation of a viscoelastic and nonlinear liver model for needle insertion

Yo Kobayashi · Akinori Onishi · Takeharu Hoshi · Kazuya Kawamura · Makoto Hashizume · Masakatsu G. Fujie

Received: 10 January 2008 / Accepted: 14 September 2008 / Published online: 28 October 2008

Abstract
Objective The objective of our work is to develop and validate a viscoelastic and nonlinear physical liver model for organ model-based needle insertion, in which the deformation of an organ is estimated and predicted, and the needle path is determined with organ deformation taken into consideration.
Materials and Methods First, an overview is given of the development of the physical liver model. The material properties of the liver considering viscoelasticity and nonlinearity are modeled based on the measured data collected from a pig's liver. The method to develop the liver model using FEM is also shown. Second, the experimental method to validate the model is explained. Both in vitro and in vivo experiments that made use of a pig's liver were conducted for comparison with the simulation using the model.
Results Results of the in vitro experiment showed that the model reproduces nonlinear and viscoelastic response of displacement at an internally located point with high accuracy. For a force up to 0.45 N, the maximum error is below 1 mm. Results of the in vivo experiment showed that the model reproduces the nonlinear increase of load upon the needle during insertion.
Discussion Based on these results, the liver model developed and validated in this work reproduces the physical response of a liver in both in vitro and in vivo situations.

Keywords Needle insertion · Physical model · Viscoelastic and nonlinear · Liver · Computer simulation

Y. Kobayashi (✉)
Consolidated Research Institute for Advanced Science and Medical Care, Waseda University, Okubo 3-4-1, Shinjuku, Tokyo 169-8555, Japan
e-mail: you-k@aoni.waseda.jp; you-k@fuji.waseda.jp

A. Onishi · T. Hoshi · K. Kawamura
Graduate School of Science and Engineering, Waseda University, Shinjuku, Japan

M. Hashizume
Center for the Integration of Advanced Medicine and Innovative Technology, Kyushu University Hospital, Fukuoka, Japan

M. G. Fujie
Graduate School of Science and Engineering, Faculty of Science and Engineering, Waseda University, Shinjuku, Japan

Introduction

Background

In recent years, research and development work has been done on surgical robots and navigation systems [1,2]. Since surgical robots are capable of minimally invasive and precise surgery, they can enhance patients' early recovery. The expectations of surgery performed by surgical robots have increased, and research and development into surgical robot systems has advanced in many fields.

One of the most common procedures employed in clinical practice is needle insertion. Recently, needle insertions, such as radiofrequency ablation (RFA) and percutaneous ethanol injection therapy (PEIT), have been used for cancer therapy. Since these treatments are based on minimally invasive surgery and achieve positive results, their future application is likely to be widespread. Recently, the need has also arisen for successful early diagnosis and treatment cancer. With this in mind, precise needle insertion will be important as an example of localized treatment for small cancers that are diagnosed early. Medical procedures such as RFA and PEIT require the insertion of a needle into a specific part of the diseased area. In all cases, the needle tip should be as close

as possible to the center of the target cancer. The needle insertion site, in the case of the liver for example, is very soft, and it is easy for the force of the needle to deform the tissues, resulting in organ deformation and displacement of the target cancer. Therefore, it is very difficult to precisely insert the needle without increasing the risk of cancer displacement.

Goal

The goal of our research was to develop an intelligent system for robot-assisted needle insertion that takes organ deformation into consideration. The functions of our method, which we call "organ model-based needle insertion" [3–7], are as follows (see Fig. 1):

(1) **Preoperative function:** Preoperative planning is carried out using the organ model to decide the optimized needle insertion path. The organ model is used to predict the organ deformation and displacement of the target cancer during needle insertion.
(2) **Intraoperative function:** A deformation calculation is carried out using intraoperative information to modify the needle path and needle speed corresponding to the state of the organ. Because intraoperative information, such as the force upon the needle measured by a force sensor, is used, real-time deformation calculation identifies the stiffness of the organ and accurately estimates organ deformation.

In short, the insertion of the needle with organ deformation taken into consideration facilitates the precise positioning of the needle tip into the target cancer. Such an intelligent system for robot-assisted needle insertion, which makes maximal use of accurate robotic positioning, will become vital in future robotic surgery, in which very precise positioning will be required. An accurate physical model of an organ that estimates and predicts the state of the real organ plays a key role in our system.

Related work

Creating an accurate organ model, which remains a challenging problem because of the complexity of organ properties, is still the subject of much research [8–21]. For example, the Physiome Project is known worldwide [9]. In addition, K. Miller presents three-dimensional, nonlinear, viscoelastic constitutive models for the liver and kidney [10], and for brain tissue [11]. Conventional research into the modeling of living bodies mainly concerns deformation analysis using a finite element method (FEM) for surgical simulation and training. For example, Tiller et al. [12] present a deformation analysis of the uterus using FEM. Alterovitz et al. [13,14] have researched the simulation of needle insertion for prostate brach therapy. Meanwhile, DiMaio and Salcudean [15,16] use a linear elastic material model to illustrate a system for measuring the extent of planar tissue phantom deformation during needle insertion. Moreover, Sakuma et al. show the equation that combines both logarithmic and polynomial strain energy forms of a pig liver from combined compression and elongation tests [17,18]. Salcudean et al. shows the planning system to determine the optimized insertion angle and position using a linear and nonlinear organ model [19,20]. Finally, Schwartz et al. [21] present a viscoelastic and nonlinear model for the simulation of needle insertion.

Purpose

In general, tissue modeling is complex because tissue exhibits inhomogeous, nonlinear, anisotropic elastic and viscous behavior [8–11,17–21]. In particular, the viscoelastic and nonlinear properties of tissue are important for precise needle insertion. It has been reported that there is nonlinear relation between the force loaded on the needle and the deformation of the liver deformation [22] as a result of nonlinear properties. It is well known that since the liver has viscoelastic properties, its deformation is dependent on the velocity of needle insertion [23].

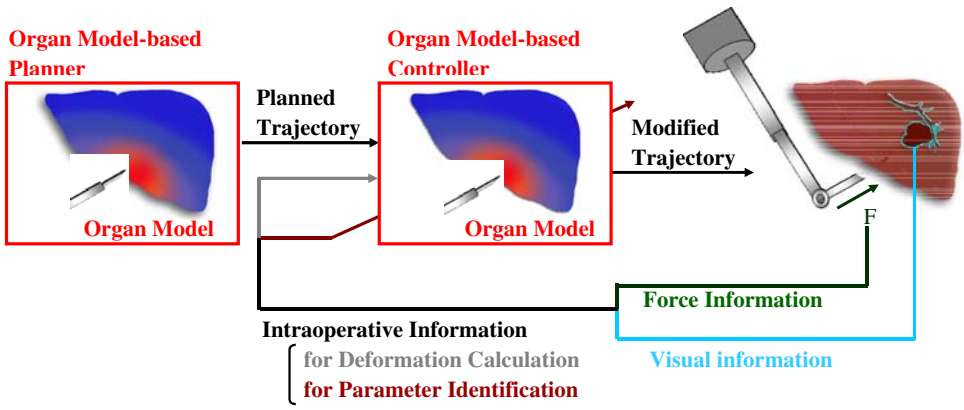

Fig. 1 The concept of organ model-based needle insertion

Our work focused on the development of a model including both viscoelastic and nonlinear properties. Schwartz et al. already present a model including viscoelastic and nonlinear properties. However, the material properties included in that model are coarse approximation of the real material properties of biological soft tissues. The uniqueness of our work is in the development of a viscoelastic and nonlinear liver model based on the detailed material properties of tissues, as well as the validation of our model based on comparing the deformation of a pig liver in both in vitro and in vivo situations. Modeling including anisotropic properties was not a target of this research, because anisotropic properties are not largely affected to the simulation of only needle insertion when the liver is compressed to a certain direction.

The rest of this paper is organized as follows: "Materials and methods I (development of physical liver model)" presents the development of our liver model, including the material properties of the model and the formulation and solution of the FEM-based model. "Materials and methods II (validation experiment)" discusses the methodology of both the in vitro and in vivo validation experiments. "Results" presents the results of these experiments. "Discussions" discusses the accuracy of our model. Finally, "Conclusion" presents a summary, overall conclusions, and a look at future work.

Materials and methods I (development of physical liver model)

Overview

In general, tissue is inhomogeneous and exhibits nonlinear, anisotropic elastic and viscous behavior, which means that tissue models are relatively complex [8]. In our work, we focused on the viscoelastic and nonlinear properties of the liver. The material properties of the liver considering both viscoelasticity and nonlinearity were modeled based on the measured data. A pig liver was used as the sample for this study because surgeons say that the abdominal organs of a pig have mechanical properties similar to those of a human's organs.

Material properties [3,4]

The material properties of a pig liver were both measured and modeled in our experiments. We have already reported on the material properties of a pig liver in [3,4], in which we also gave specific descriptions of the physical properties of the liver. Thus, only a simplified explanation of the material behavior used for deformation calculation is shown in this paper.

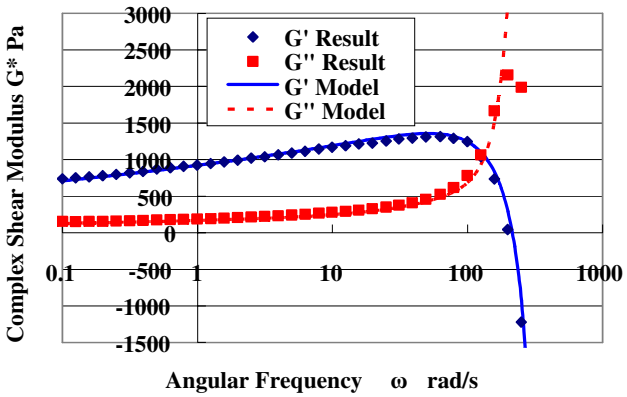

Fig. 2 Mechanical impedance of the liver [3–6]

Experiments were individually implemented to measure the physical properties of the pig's interior liver using a rheometer (TA-Instrument: AR550). The shear modulus, shear stress, and shear strain were then calculated based on these results.

Viscoelastic properties

A dynamic viscoelastic test was carried out to measure the frequency response of the liver. A sine-wave stress from 0.1 to 250 rad/s, providing 3% strain amplitude, was loaded on the liver, and a dynamic viscoelastic test was conducted. The mechanical impedance of the pig liver obtained from the result of this test is shown in Fig. 2. G* is a complex shear modulus, G' the storage elastic modulus, and G" the loss elastic modulus. The needle is generally inserted into the organ at a low velocity; hence the response is mainly affected by the low frequency characteristics. Thus, we used the viscoelastic model using the fractional derivative described in (1), which takes only low-frequency characteristics into consideration.

$$G\frac{\mathrm{d}^k\gamma}{\mathrm{d}t^k} = \tau \tag{1}$$

where G is the viscoelasticity, k is the order of derivative, γ is the shear strain, t is time, and τ is the shear stress. The derivative order k was approximately equal to 0.1, based on the slopes of G' and G'' shown in Fig. 2.

Nonlinear properties (*strain dependence of elastic modulus*)

The nonlinear characteristics of liver as a material were investigated based on the creep test, in which the step response is measured. The steady state of the step response following sufficient elapsed time exhibits the low-frequency characteristics described in (1). And, Eq. (1) becomes (2) if (1) is solved by the condition of the creep test.

$$\gamma = \frac{\tau_c}{G\Gamma(1+k)}t^k = \gamma_c t^k \tag{2}$$

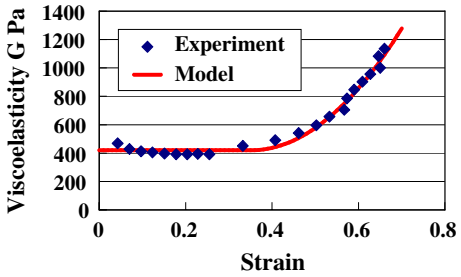

Fig. 3 Strain dependence of Viscoelasticity [3–6]

where τ_c is constant shear stress, $\Gamma()$ is the gamma function, t is time, and γ_c is the coefficient deciding the strain value.

The creep test for each stress was carried out repeatedly while the viscoelasticity G and strain γ_c or each stress were calculated using (2). Figure 3 shows the viscoelasticity G-strain γ_c diagram from these results. A liver with a low strain of less than about 0.35 displays linear characteristics and a viscoelasticity G at a constant 400 Pa. A liver with a high strain of more than about 0.35 displays nonlinear characteristics and an increased degree of viscoelasticity G. Then, strain dependence was modeled using the quadratic function of strain shown by (3)

$$G(\gamma) = \begin{cases} G_o & (\gamma < \gamma_0) \\ G_0(1 + a_\gamma\,(\gamma - \gamma_0)^2) & (\gamma > \gamma_0) \end{cases} \tag{3}$$

where G_o is the viscoelastic modulus of the linear part, a_γ is the coefficient deciding the change of stiffness, and γ_0 is the strain at which the characteristics of the liver change to show nonlinearity.

Shear stress-strain relation

The material properties of the liver were modeled using (4) from the discussion in "Viscoelastic properties" and "Nonlinear properties (strain dependence of elastic modulus)".

$$G(\gamma)\frac{\mathrm{d}^k\gamma}{\mathrm{d}t^k} = \tau \tag{4}$$

Stress-strain relation

In general, the elastic modulus E was used to construct the deformation model. The relation between the elastic modulus E and the shear modulus G was calculated using Poisson's ratio ν as in the following equation:

$$E = 2(1 + \nu)\,G \tag{5}$$

In the experiment using the rheometer, only the shear modulus was loaded on the test material. However, the stress state is more complex in the situation of deformation simulation. We assume that the nonlinearity of the elastic modulus is decided by the relative strain calculated in (6).

$$\varepsilon_r = \sqrt{\frac{2}{9}\left\{(\varepsilon_1 - \varepsilon_2)^2 + (\varepsilon_2 - \varepsilon_3)^2 + (\varepsilon_3 - \varepsilon_1)^2\right\}} \tag{6}$$

where $\varepsilon_1, \varepsilon_2, \varepsilon_3$ is the principal strain.

Thus, from these considerations, the material properties using the liver model are described in (7) and (8).

$$E(\varepsilon_r)\frac{\mathrm{d}^k\varepsilon}{\mathrm{d}t^k} = \sigma \tag{7}$$

$$E(\varepsilon) = \begin{cases} E_o & (\varepsilon < \varepsilon_0) \\ E_0(1 + a_\varepsilon\,(\varepsilon_r - \varepsilon_0)^2) & (\varepsilon > \varepsilon_0) \end{cases} \tag{8}$$

FEM based liver model [5,6]

This section shows the formulation and solution to the FEM model using the material properties described in "Material properties [3,4]". We already have reported the formulation and solution to the FEM model and already have given specific descriptions in [5,6]. Thus, only a simplified explanation for the solution is shown in this paper.

The expression between the displacements at all the nodal points and all the applied loads is written in (9)–(11) from the result of (8).

$$\mathbf{K}(\mathbf{U})D^{(k)}\mathbf{U} = \mathbf{F} \tag{9}$$

where

$$\mathbf{K}\,(\mathbf{U}) = \sum_{\text{all element}} \mathbf{k}\,(\varepsilon_r) \tag{10}$$

$$\mathbf{k}(\varepsilon_r) = \begin{cases} \mathbf{k_0} & (\varepsilon_r < \varepsilon_0) \\ \mathbf{k_0}(1 + a_\varepsilon\,(\varepsilon_r - \varepsilon_0)^2) & (\varepsilon_r > \varepsilon_0) \end{cases} \tag{11}$$

where $\mathbf{k}$ is the nonlinear element stiffness matrix, $\mathbf{k_0}$ is the element stiffness matrix when the liver tissue shows linear characteristics, a_ε is the coefficient deciding the change of stiffness, and ε_r is the relative strain.

First, the solution for the viscoelastic system is shown in "Solution for the viscoelastic system", and the solution for the nonlinear system is given in "Nonlinear system". Finally, the solution for (9) is shown based on the discussions from both "Solution for the viscoelastic system" and "Nonlinear system".

Solution for the viscoelastic system

The analysis can be considerably simplified when the following conditions are fulfilled [24]:

- The derivative operator of (9) is a common factor in all element stiffness.
- Only the external loads influence the stresses.

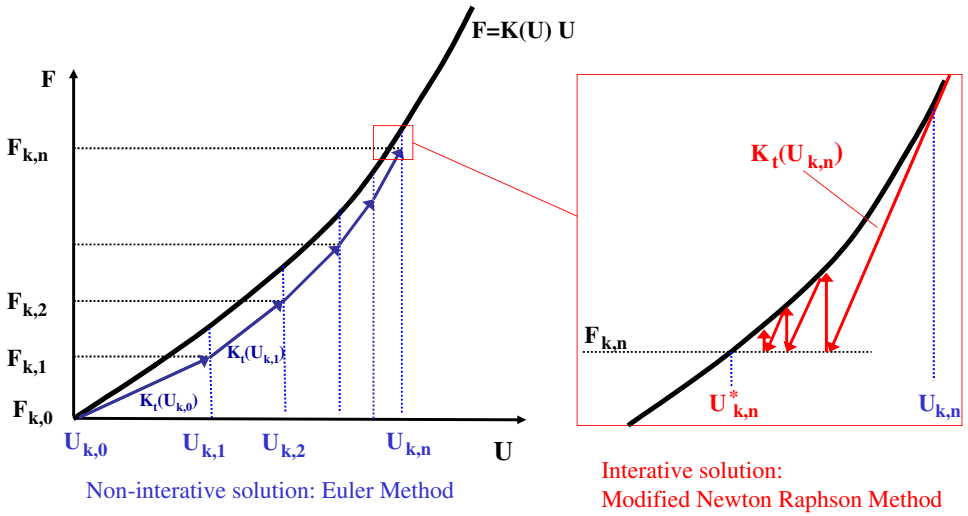

Fig. 4 The solution to the nonlinear FEM equation

Then, Eq. (12) is derived from (9).

$$\mathbf{K}(\mathbf{U})\mathbf{U} = \mathbf{F}' \quad \left(\mathbf{F}' = D^{(-k)}\mathbf{F}\right) \tag{12}$$

where $D^{(-k)}$ means the kth-order integration.

Equation (12) is identical to the elastic problem when the virtual external force vector $\mathbf{F}'$ is used. The fractional calculation (12) for each component of the external force vector $\mathbf{F}$ was implemented to obtain the virtual external force vector $\mathbf{F}'$. We used the sampling time scaling property introduced in [5,6,25] to make a discrete fractional calculation. The sampling time scaling property was the method we used to consider the discrete fractional order integrals as the "deformation" of their integer order counterparts.

Nonlinear system

Incremental approaches are important to obtain a significant answer because the answer is not unique for many nonlinear situations. The incremental form of a discrete nonlinear model is generally written by as in (13).

$$\mathbf{K_t}(\mathbf{U_n})\Delta U_\mathbf{n} = \Delta F_\mathbf{n} \tag{13}$$

where $\mathbf{K}_t$ is the tangential stiffness matrix, $\Delta\mathbf{U}_n$ is an increment of the overall displacement vector, and $\Delta\mathbf{F}_n$ is an increment of the overall external force.

The tangential matrix $\mathbf{K}_t$ is described by (14) from Eq. (11).

$$\mathbf{K_t}(\mathbf{U}) = \sum_{\text{all element}} \mathbf{k_t}(\boldsymbol{\varepsilon_r}) \tag{14}$$

$$\mathbf{k}_t(\varepsilon_r) = \begin{cases} \mathbf{k_0} & (\varepsilon_r < \varepsilon_0) \\ \left[1 + a_\varepsilon(\varepsilon_r - \varepsilon_0)^2 + 2a_\varepsilon(\varepsilon_r - \varepsilon_0)\varepsilon_r\right]\mathbf{k_0} & (\varepsilon_r > \varepsilon_0) \end{cases} \tag{15}$$

where $\mathbf{k}_t$ is the tangential element stiffness matrix.

We used both the Euler method and the Modified Newton–Raphson method to solve the nonlinear system, as shown in Fig. 4.

Calculation process

Based on these discussions, the solution for the system (9) can be described as follows. First, the virtual external force $\mathbf{F}'$ was calculated, then the incremental of $\mathbf{F}'(\Delta\mathbf{F}')$ was computed. The solution to the nonlinear system described in "Nonlinear properties (strain dependence of elastic modulus)" was then carried out using $\Delta\mathbf{F}'$.

$$\mathbf{K}(\mathbf{U_n})\,\Delta\mathbf{U_n} = \Delta\mathbf{F}'_\mathbf{n} \tag{16}$$

Materials and methods II (validation experiment)

Validation of liver model by in vitro experiment

Measurement of liver deformation

Some researchers have shown the methods for the measuring of organ deformation. For example, DiMaio et al. [15] measured the deformation of a liver or phantom by sensing the displacement of a marker attached to the surface. However, there is a significant difference between the deformation of the liver surface to which the marker is attached and the deformation of the liver in the needle plane.

In our work, medical ultrasound equipment was used to measure the deformation of the liver in the needle plane. Medical ultrasound equipment was selected from the various diagnostic imaging systems because it can provide the time-series data required to validate the viscoelastic properties.

Following are the experimental setup and conditions (also see Fig. 5). The deformation of the liver was measured from recognition of the ultrasound image. Part of the liver wall

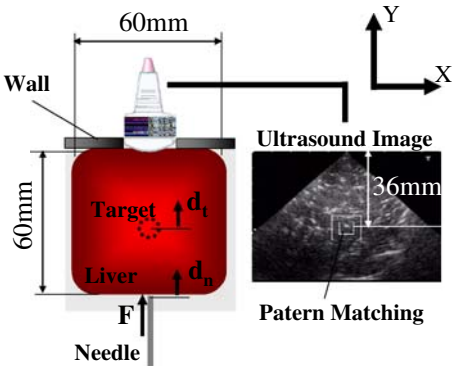

Fig. 5 Concept of the experimental setup

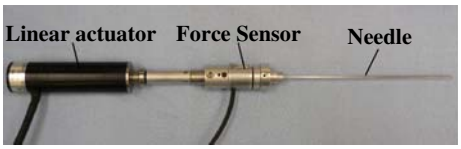

Fig. 6 Needle insertion unit

was perforated, and the medical ultrasound equipment was set into the perforation. This setup prevented any liver deformation caused by the ultrasound probe coming into contact with the liver. The probe of the medical equipment was placed in needle insertion plane. The ultrasound images of the liver included various special features because of the presence of various tissues such as fat. The feature point on the ultrasound image is the virtual target that represents the cancer, and pattern recognition (normal correlation) was carried out to measure the position of the virtual target. The white-box in the ultrasound image in Fig. 5 shows the measured point, and the initial length between the measured point and the wall was 36 mm.

The liver was cut into a rectangular solid (60 × 60 mm, thickness 20 mm), and the rear side of the liver was constrained by the wall. The liver was attached to sandpaper using glue, and the sandpaper was attached to the wall using double-sided tape. A dimensional outline drawing of the liver is shown in Fig. 5.

A 17-gauge, bevel-tip needle used for biopsy purposes was used for the experiment. The needle was attached to the linear actuator used to insert the needle. A six axis load cell was attached to the tip of the linear actuator to measure the force loaded onto the needle. Figure 6 shows the needle insertion unit.

The needle was inserted from the center of the liver surface (Fig. 5). The axial force loaded onto the needle in the Y direction was controlled equal to the target force, which was set to increase linearly, by 0.45 N at 0.025 N/s during the first 18 s. Subsequently, the target force was set to a constant force at 0.45 N for 30 s. The nonlinear property of the liver was evaluated based on the liver's response during linear increase, and the viscoelastic property of the liver was evaluated based on the liver's response during constant force.

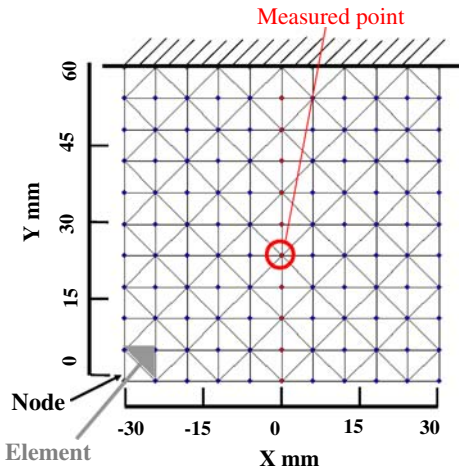

Fig. 7 Model shape of the deformation evaluation

Then, the time-series data of the displacement of the needle and of the virtual target was collected.

We used the measurement of displacement at a single point in the liver to validate the liver model. In future work, we will use a large number of measurement points to validate the overall deformation of the liver model.

Model deformation

A 2-D slice of the liver model was defined using mesh triangular elements. Figure 7 shows the initial shape of the FEM liver model. This model shape is the same as the shape of the liver used in the experiment, and the rear side of model is set to be the fixed end. This model has 121 total nodes, 200 total elements, and a 20 mm thickness. The stiffness parameters of the model such as G_o, ε_0, and a_ε were set manually to fit the measured data presented in "Measurement of liver deformation".

It was assumed that the needle was inserted into the center of the liver model at $(X, Y) = (0, 0)$ mm (see Fig. 7), while the force was ordered to load the node at (0.0, 0.0) mm in the Y direction. The ordered force was set to increase linearly, by 0.45 N at 0.025 N/s during the first 18 s. Subsequently, the target force was set to a constant force at 0.45 N for 30 s.

The time-series data of the displacement of both the needle and the virtual target were collected during the numerical experiment. The initial position of the virtual target was set to be the same as the measured point in the experiment, as described in "Measurement of liver deformation".

Validation of liver model by in vivo experiment

In vivo experiment

We also evaluated our liver model by an in vivo experiment using a pig liver. The needle was inserted into a pig liver

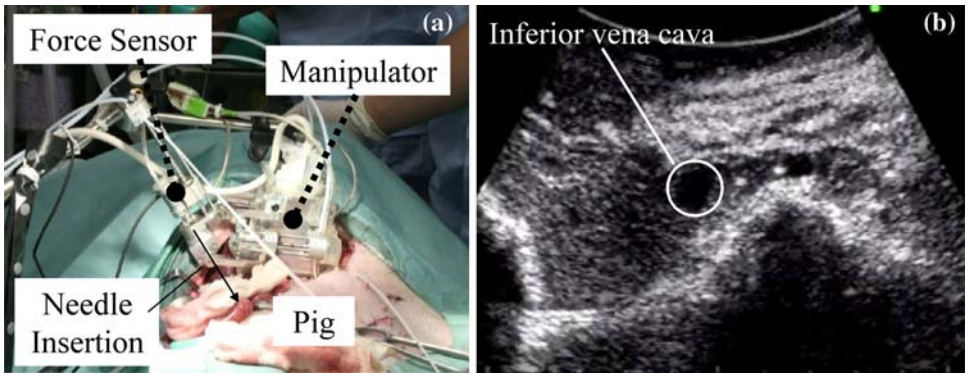

Fig. 8 Experimental setup of in vivo experiment

at a constant velocity of 5 mm/s using a needle insertion manipulator with the medical ultrasound equipment (Fig. 8a). The inferior vena cava in the liver, as shown in Fig. 8b, was set to be the virtual target of this experiment. Then, the needle displacement and force during needle insertion were collected, and ultrasound images were captured.

Since the needle was inserted at a constant velocity, this experiment may primarily show the nonlinear properties of the liver rather than the viscoelastic properties. Therefore, this validation mainly evaluates the nonlinear properties of the liver model.

Analysis using liver model

Considering the size of a pig liver, the shape of the liver model developed for the in vivo evaluation was assumed to be a square (70×70 mm). The mesh and coordinate system of the liver model were the same as for the in vitro experiment (Fig. 6). The rear side of model was set to be the fixed end, because the rear side of pig liver is considered to be constrained by the abdominal wall of the back side. The stiffness of the element in the inferior vena cava part was set to approximately 0 Pa, because the actual stiffness of the inferior vena cava part is very low compared to that of normal tissue. The stiffness parameters such as E_o, ε_0, and a_ε of the normal tissue part were set manually to fit the data of the experiment. Again, it was assumed that the needle was inserted at the center of the liver model at $(X, Y) = (0, 0)$ mm, and that it was inserted at a constant speed of 5 mm/s in the Y direction. The time-series data of needle displacement and of the force loaded on the needle were collected during the numerical experiment. Only the initial loading phase was analyzed in this numerical simulation. A simulation including puncture phenomenon will be carried out in the near future.

To evaluate the presence of blood vessels, we also developed a homogeneous liver model without the blood vessel part, and simulation was carried out under the same conditions.

Because the real shape of a pig liver is not rectangular and since the real boundary conditions are more complex as a matter of course, the validation of our liver model was not rigorous. In the future, a more rigorous deformation analysis should be carried out, one that uses a liver model that captures the shape and boundary conditions of a real pig liver.

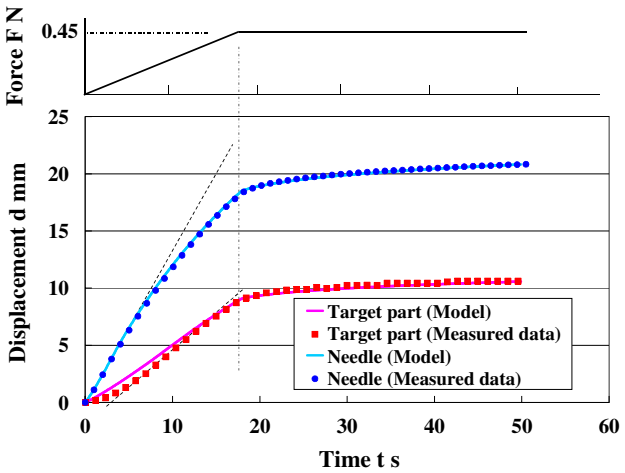

Fig. 9 Experimental and simulation result of liver deformation

Results

Results of in vitro experiment

Figure 9 shows the experimental results of liver deformation, both the time-series data of needle displacement and virtual target displacement as measured by the experiment presented in "Measurement of liver deformation", and the time-series data of needle displacement and virtual target displacement on the model. Figure 10 shows the overall model deformation and distribution of the Mises stress of each element. The color of each element in Fig. 10 indicates the value of the stress.

Results of in vivo experiment

Figure 11 shows the relation between needle displacement and force on the real liver and liver model (both with and without the blood vessel), whereas the simulation data shown

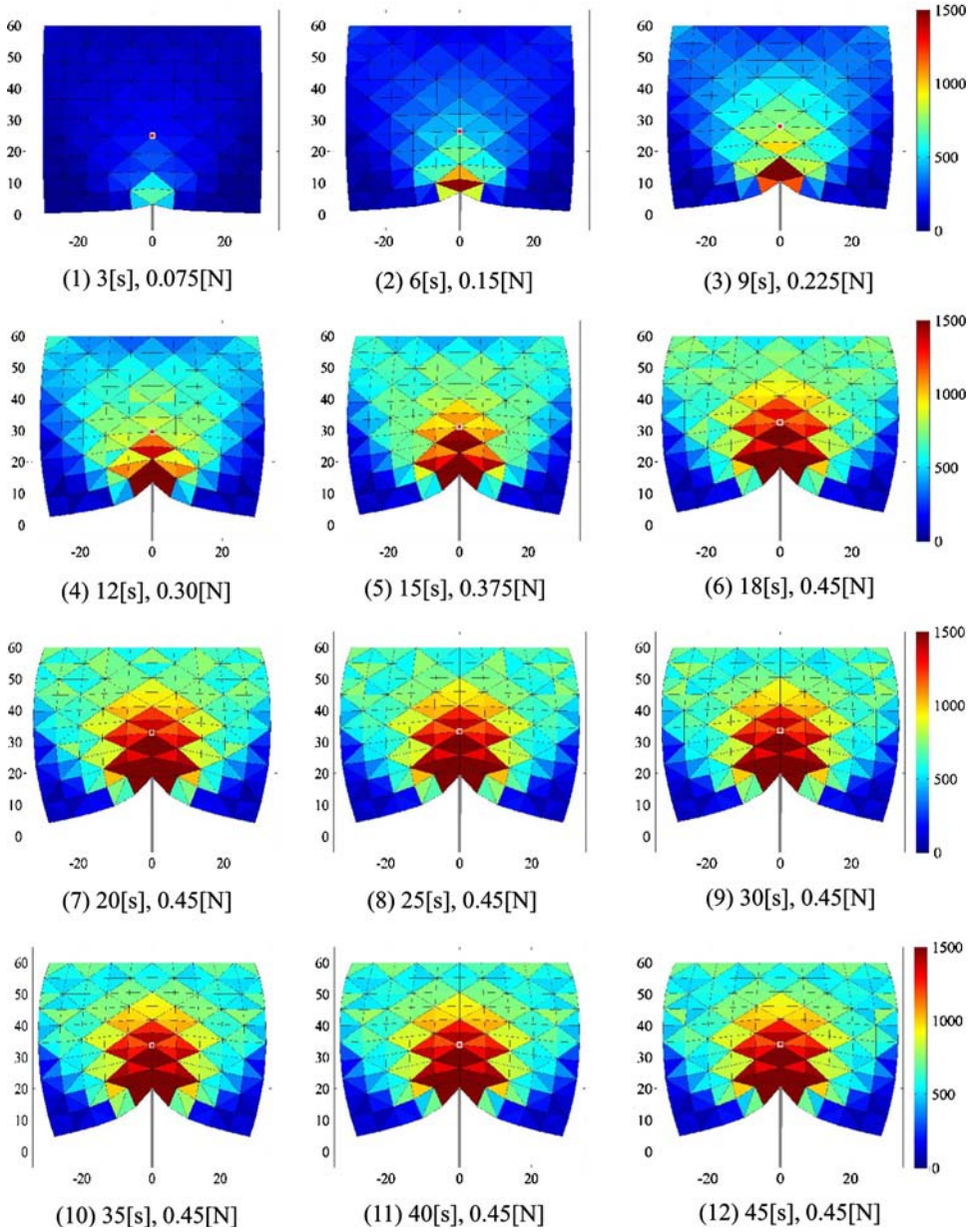

Fig. 10 Model deformation for model evaluation

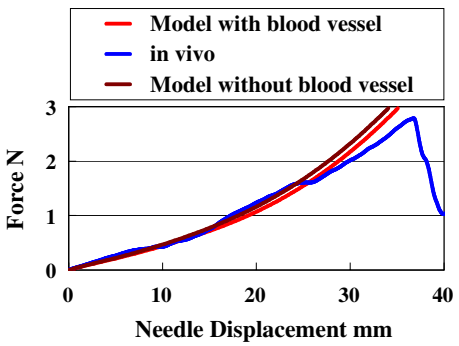

Fig. 11 Relationship between needle displacement and force: in vivo experiment

in Fig. 11 displays only the initial loading phase. Figure 12 shows the deformation of the liver model both with the blood vessel and without the blood vessel; it also shows the ultrasound images captured during the in vivo experiment.

Discussions

In vitro experiment

Needle displacement (0–18 s)

The needle displacement in Fig. 9 increased linearly when the loaded force was small (0–5 s); however, it showed a low

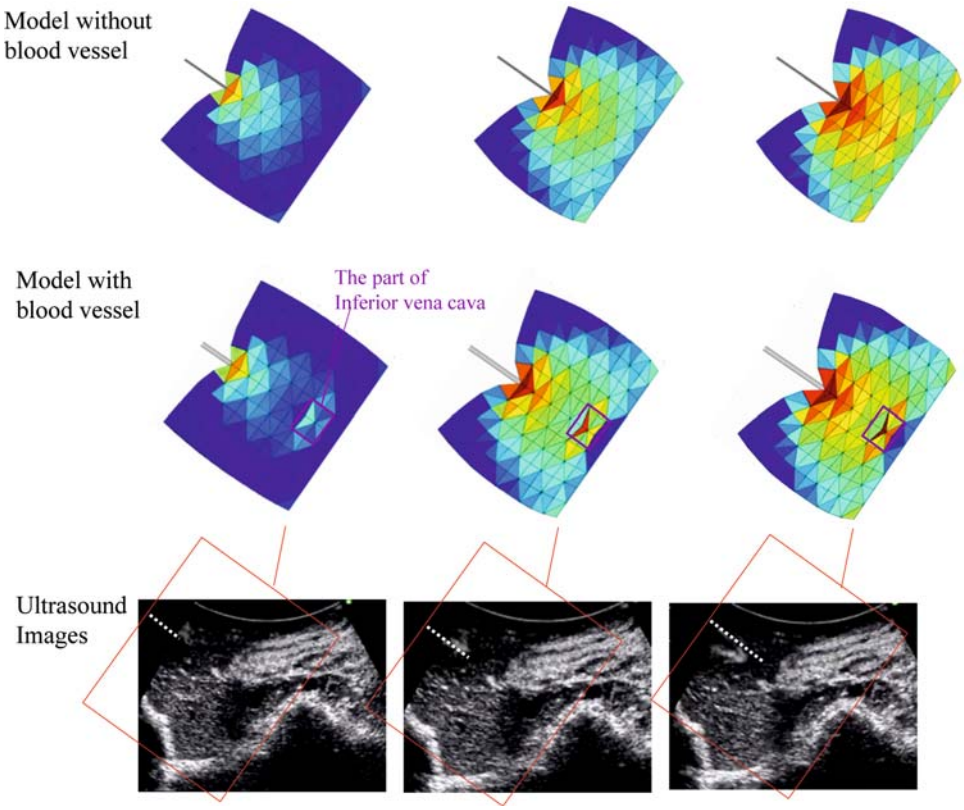

Fig. 12 The comparison of model deformation with the ultrasound image

increase rate when the loaded force was large (5–18 s). This result stems from the nonlinear characteristics of liver, that is, liver subject to high strain displays features of rigidity whereas liver subject to lower strain does not, as shown in Fig. 3.

Based on the results from the liver model, it is clear that needle displacement also showed linear increase when subjected to a small force (0–5 s) and a low increase rate when the loaded force was large (5–18 s). And, Fig. 9 shows that the liver model reproduced the nonlinear response of a real liver with high accuracy.

Needle displacement (18–50 s)

Needle displacement increased after the loaded force was set to be constant (18–50 s). This result is related to the viscoelastic characteristics of the liver, as shown in "Material properties [3,4]", while the strain on the liver increased with constant stress, as shown in Eq. (2).

The results from the liver model also show that needle displacement increased during constant force (18–50 s), while Fig. 9 shows that the liver model reproduced the viscoelastic response of the real liver with high accuracy.

Displacement of virtual target (0–18 s)

The virtual target displacement increased with acceleration in the early stages of load application (0–5 s). First, the rate of displacement was low, but then it increased rapidly. In addition, the displacement of the virtual target (see Fig. 9) increased linearly when the loaded force was small (5–15 s), while it increased nonlinearly when the loaded force was large(15–18 s).

As shown in Fig. 9, the model results of the virtual target show an accelerating increase in displacement. Although the model results have about 1 mm error when comparing the data measured by the real organ in the early stage of applying a load (0–5 s), the error diminishes corresponding to the increase of loaded force. The liver model reproduced with high accuracy the nonlinear response of displacement at an internally-located point shown in the real liver when the loaded force was considerable (12–18 s).

Displacement of virtual target (18–50 s)

The displacement of an internally-located virtual target in the liver also increased after the loaded force was set to be constant (18–50 s).

The results from the liver model also show that the displacement of the virtual target increased during constant force (18–50 s). Then, as shown in Fig. 9, our liver model reproduced with high accuracy the viscoelastic response of displacement at an internally-located point shown in the real liver.

In vivo experiment

Results of the in vivo experiment are shown in Fig. 11. There is a nonlinear relation between needle displacement and force. The liver model with the blood vessel reproduced with high accuracy the relation between needle displacement and force of the in vivo liver. In the simulation, the model with the blood vessel shows a little smaller force increase than the model without the blood vessel. This result is due to the low elasticity of the blood vessel part.

The ultrasound images in Fig. 12 show that the inferior vena cava in the liver collapsed from the force of the needle that the part of the inferior vena cava in the liver model with the blood vessel also collapsed, in contrast to the model without the blood vessel.

Based on all these results, we consider that our liver model also reproduces the in vivo situation.

Parameter variation

Table 1 gives the values of all the stiffness parameters. Table 1a shows the parameters obtained from the experiment for the modeling of the material properties discussed in "Materials and methods I (development of physical liver model)". Table 1b shows the parameters of the model for the in vitro experiment, while Table 1c shows the parameters of the model for the in vivo experiment.

There is a large variation between each stiffness parameter in (a) and that in (b), even though both sets of data were obtained from the in vitro tissue. In general, the material parameters of tissues vary as the result of individual differences in a number of individual factors such as age, gender, living habits, etc. The differences between the stiffness parameters in (a) and (b) are assumed to be the result of these individual differences. This discussion leads to the conclusion that both parameter identification methods such as previous work [7] and the evaluation of parameter variation from a large number of individuals are both necessary for the clinical application of any model such as ours.

There also are large differences between the stiffness parameters when the data of (a) and (b) are compared with (c). These differences may be caused by the differences between the in vitro liver and the in vivo liver. It is said that the in vivo liver is harder than the in vitro liver because the in vivo liver has more blood in blood vessels than the in vitro liver. As a result, the stiffness parameters of the in vivo liver must be evaluated for clinical application.

Table 1 Stiffness parameters

Experiment	G_o	ε_0	a_ε
(a)	1,200	0.1	21,000
(b)	2,600	0.15	45,000
(c)	5,000	0.1	3,00,000

Conclusion

We developed and validated a viscoelastic and nonlinear liver deformation model for organ model-based needle insertion. First, the concept of organ model-based needle insertion was described, and then the importance of the organ model, including detailed material characteristics, was shown. Second, we used FEA to model the detailed material properties of the liver based on the measured data. Both in vitro and in vivo-experiments were carried out for comparison with the simulation using the model. The needle displacement and displacement at an internally-located point in the real liver were measured, and the displacement of the liver model was calculated. Comparing the measurement data of the real liver with that of the liver model, we validated the model.

The results of the in vitro experiment showed that the liver model reproduced with high accuracy the nonlinear and viscoelastic response of displacement at an internally-located point in the liver. The maximum displacement error was about 1 mm for a force up to 0.45 N. The results of the in vitro experiment showed that the model reproduced the nonlinear increase of load upon the needle during insertion.

From these results, we consider that the liver model we developed accurately reproduced the physical response of the liver in both in vitro and in vivo situations. This accurate reproduction suggests that the method we used to develop the physical liver model is useful to simulate needle insertion into the liver.

In future, further precise liver modeling will be carried out to realize more accurate needle insertion. Liver modeling including anisotropic properties will be carried out; this kind of modeling was not a target of this research because anisotropic properties, compared with viscoelasticity and nonlinearity, do not have a large effect on the simulation when the liver is compressed in a certain direction. In addition, a liver model should be developed that considers inhomogeneous properties when the target is a liver affected by disease, including hepatic cirrhosis. Detailed inhomogeneous modeling that takes hepatic cirrhosis into account should be carried out. And, the accurate setting of liver shape and boundary conditions also will be carried out. First, a liver model with the actual shape and complex boundary conditions of a real pig liver should be validated so it can be used for more detailed evaluations. Then, it should be determined whether the proposed liver model can be generalized to human liver tissue. The model parameter identification method using intra-operative information will also be researched, with reference to the ambiguity of the model parameter. Finally, the

organ model-based needle insertion system will be further developed for use in safe and precise clinical treatment.

Acknowledgments This work was supported in part by the 21st Century Center of Excellence (COE) Program "The innovative research on symbiosis technologies for human and robots in the elderly dominated society", Waseda University, Tokyo, Japan, and in part by "Establishment of Consolidated Research Institute for Advanced Science and Medical Care", Encouraging Development Strategic Research Centers Program, the Special Coordination Funds for Promoting Science and Technology, Ministry of Education, Culture, Sports, Science and Technology, Japan and in part by "the robotic medical technology cluster in Gifu prefecture," Knowledge Cluster Initiative, Ministry of Education, Culture, Sports, Science and Technology, Japan.

References

1. Taylor RH, Stoianovici D (2003) Medical robotics in computer-integrated surgery. IEEE Trans Robot Autom 19(5):765–781. doi:10.1109/TRA.2003.817058
2. Daraio P, Hannaford B, Menciassi A (2003) Smart surgical tools and augmenting devices. IEEE Trans Robot Autom 19(5):782–792. doi:10.1109/TRA.2003.817071
3. Kobayashi Y, Okamoto J, Fujie MG (2004) Physical properties of the liver for needle insertion control. In: IEEE international conference on intelligent robotics and systems, pp 2960–2966
4. Kobayashi Y, Okamoto J, Fujie MG (2005) Physical properties of the liver and the development of an intelligent manipulator for needle insertion. In: IEEE international conference on robotics and automation, pp 1644–1651
5. Kobayashi Y, Onishi A, Hoshi T, Kawamura K, Fujie MG (2007) Viscoelastic and nonlinear organ model for control of needle insertion manipulator. In: IEEE international conference of the EMBS, pp 1893–1899
6. Kobayashi Y, Onishi A, Hoshi T, Kawamura K, Fujie MG (2007) Deformation simulation using a viscoelastic and nonlinear organ model for control of a needle insertion manipulator. In: IEEE international conference on intelligent robotics and systems, pp 1801–1808
7. Hoshi T, Kobayashi Y, Kawamura K, Fujie MG (2007) Developing an intraoperative methodology using the finite element method and the extended kalman filter to identify the material parameters of an organ model. In: Proceeding of the 29th international conference of the ieee engineering in medicine and biology society, pp 469–474
8. Famaey N, Sloten JV Soft tissue modelling for applications in virtual surgery and surgical robotics. Comput Methods Biomech Biomed Eng 11:4, pp. 351–366
9. The IUPS Physiome Project. http://www.bioeng.auckland.ac.nz/physiome/physiome_project.php
10. Miller K, Chinzei K, Orssengo G, Bednarz P (2000) Mechanical properties of brain tissue in vivo: experiment and computer simulation. J Biomech 33:1369–1376
11. Miller K (2000) Constitutive modelling of abdominal organs. J Biomech 33(3):367–373
12. Tillier Y, Paccini A, Durand-Reville M, Bay F, Chenot JL (2003) Three-dimensional finite element modeling for soft tissues surgery. Comput Assist Radiol Surg, pp 349–355
13. Alterovitz R, Lim A, Goldberg K, Chirikjian GS, Okamura AM (2005) Steering flexible needles under markov motion uncertainty. In: IEEE international conference on intelligent robots and systems, pp 120–125
14. Alterovitz R, Goldberg K, Okamura A (2005) Planning for steerable bevel-tip needle insertion through 2D Soft tissue with obstacles. In: IEEE international conference on robotics and automation, pp 1652–1657
15. DiMaio SP, Salcudean SE (2003) Needle insertion modelling and simulation. IEEE Trans Robot Autom 19(5):864–875. doi:10.1109/TRA.2003.817044
16. DiMaio SP, Salcudean SE (2005) Interactive simulation of needle insertion model. IEEE Trans Biomed Eng 52(7):1167–1179. doi:10.1109/TBME.2005.847548
17. Goksel O, Salcudean SE, DiMaio SP, Rohling R, Morris J (2005) 3D needle-tissue interaction simulation for prostate brachytherapy. In: Medical image computing and computer-assisted intervention, pp 827–834
18. Dehghan E, Salcudean SE (2007) Needle insertion point and orientation optimization in non-linear tissue with application to brachytherapy. In: IEEE international conference on robotics and automation, pp 2267–2272
19. Sakuma I, Nishimura Y, Chui CK, Kobayashi E, Inada H, Chen X, et al (2003) In vitro measurement of mechanical properties of liver tissue under compression and elongation using a new test piece holding method with surgical glue. In: Proccedings on international symposium IS4TM, pp 284–292
20. Chui C, Kobayashi E, Chen X, Hisada T, Sakuma I (2006) Combined compression and elongation experiments and nonlinear modelling of liver tissue for surgical simulation. Med Biol Eng Comput 42(6):787–798. doi:10.1007/BF02345212
21. Schwartz JM, Denninger M, Rancourt D, Moisan C, Laurendeau D (2005) Modelling liver tissue properties using a nonlinear viscoelastic model for surgery simulation. Med Image Anal 9(2):103–112
22. Okamura AM, Simone C, O'Leary MD (2004) Force modeling for needle insertion into soft tissue. IEEE Trans Biomed Eng 51(10):1707–1716. doi:10.1109/TBME.2004.831542
23. Heverly M, Dupont P, Triedman J (2005) Trajectory optimization for dynamic needle insertion. In: IEEE international conference on robotics and automation, pp 1646–1651
24. Zienkiewicz OC, Cheung YK (1967) The finite element method in structural and continuum mechanics. McGraw-Hill Publ. Co., New York
25. Ma C, Hori Y (2004) The application of fractional order control to backlash vibration suppression. In: Proceedings of american control conference, pp 2901–2906